

# Faint extended Ly $\alpha$ emission due to star formation at the centre of high column density QSO absorption systems

Luke A. Barnes<sup>\*</sup> and Martin G. Haehnelt

*Institute of Astronomy and Kavli Institute for Cosmology, Madingley Road, Cambridge, CB3 0HA*

not yet submitted

## ABSTRACT

We use detailed Ly $\alpha$  radiative transfer calculations to further test the claim of Rauch et al. (2008) that they have detected spatially extended faint Ly $\alpha$  emission from the elusive host population of Damped Ly $\alpha$  Absorption systems (DLAs) in their recent ultra-deep spectroscopic survey. We investigate the spatial and spectral distribution of Ly $\alpha$  emission due to star-formation at the centre of DLAs, and its dependence on the spatial and velocity structure of the gas. Our model simultaneously reproduces the observed properties of DLAs and the faint Ly $\alpha$  emitters, including the velocity width and column density distribution of DLAs and the large spatial extent of the emission of the faint emitters. Our modelling confirms previous suggestions that DLAs are predominately hosted by Dark Matter (DM) halos in the mass range  $10^{9.5} - 10^{12} M_{\odot}$ , and are thus of significantly lower mass than those inferred for  $L_*$  Lyman Break Galaxies (LBGs). Our modelling suggests that DM halos hosting DLAs retain up to 20% of the cosmic baryon fraction in the form of neutral hydrogen, and that star formation at the centre of the halos is responsible for the faint Ly $\alpha$  emission. The scattering of a significant fraction of the Ly $\alpha$  emission to the observed radii, which can be as large as 50kpc or more, requires the amplitude of the bulk motions of the gas at the centre of the halos to be moderate. The observed space density and size distribution of the emitters together with the incidence rate of DLAs suggests that the Ly $\alpha$  emission due to star formation has a duty cycle of  $\sim 25\%$ .

**Key words:** quasars: absorption lines — galaxies: formation

## 1 INTRODUCTION

Rauch et al. (2008, hereafter R08) recently reported the results of an ultra-deep spectroscopic survey for low surface brightness Ly $\alpha$  emitters at redshift  $z \sim 3$ . A 92 hour long exposure with the ESO VLT FORS2 instrument yielded a sample of 27 faint line emitters with fluxes of a few times  $10^{-18}$  erg s $^{-1}$  cm $^{-2}$ , which they argue are likely to be dominated by Ly $\alpha$ . They further conclude that the large comoving number density,  $3 \times 10^{-2} h_{70}^3$  Mpc $^{-3}$ , and the large covering factor  $dN/dz \sim 0.2 - 1$  suggest that the emitters can be identified with the elusive host population of damped Ly $\alpha$  systems (DLAs) and high column density Lyman limit systems. Barnes & Haehnelt (2009, hereafter BH09), building on the successful model for DLAs of Haehnelt, Steinmetz, & Rauch (1998, 2000), presented a simple model that simultaneously accounts for the kinematic properties and incidence rate of the observed DLAs *and* the luminosity function and the size distribution of the R08 emitters in the context of the  $\Lambda$ CDM

model for structure formation. The model assumes a simple relation between the size of the damped absorption and Ly $\alpha$  emission regions, and proposes that the Ly $\alpha$  luminosity is proportional to the total halo mass. BH09 further corroborated the suggestion that cooling radiation is not expected to contribute significantly to the observed Ly $\alpha$  emission, and that the emitters are most likely powered by star formation. In the model, DLAs are small galaxies hosted by DM halos with masses in the range  $10^{9.5}$  to  $10^{12} M_{\odot}$  and have rather large low surface brightness Ly $\alpha$  halos which extend to radii of up to 50kpc or larger.

In order to fit the observed size distribution of the faint Ly $\alpha$  emitters, BH09 assumed that the Ly $\alpha$  emission extends to radii somewhat larger than is required to reproduce the incidence rate for DLAs. However, no modelling of the gas distribution and Ly $\alpha$  radiative transfer was done. We present such modelling here to investigate whether the sizes, surface brightness profiles and spectral line shapes can be reproduced with simple but plausible assumptions for the distribution and the physical properties of the gas in the DM halos suggested by our previous modelling to be the hosts of the faint emitters.

<sup>\*</sup> E-mail: lab@ast.cam.ac.uk (LAB); haehnelt@ast.cam.ac.uk (MGH)

Studies of the radiative transfer of Ly $\alpha$  have a long history. The first investigations employed approximate calculations and simple physical arguments (Zanstra 1949; Unno 1952; Osterbrock 1962; Adams 1971, 1972). Later, analytic solutions were found for simple geometries in the limit of large optical depth (Harrington 1973; Neufeld 1990). It was realised early, however, that Monte Carlo simulations provided the most flexible method for investigating arbitrary geometry, density distributions and velocity structures. Many investigations have employed such techniques - Avery & House (1968); Auer (1968); Caroff, Noerdlinger, & Scargle (1972); Panagia & Ranieri (1973); Bonilha et al. (1979); Natta & Beckwith (1986); Ahn, Lee, & Lee (2000, 2001, 2002); Zheng & Miralda-Escudé (2002); Cantalupo et al. (2005); Hansen & Oh (2006); Tasitsiomi (2006), Dijkstra, Haiman, & Spaans (2006, hereafter DHS06), Verhamme, Schaerer, & Maselli (2006); Laursen, Razoumov, & Sommer-Larsen (2009).

Our modelling is most similar to that of DHS06 and Verhamme, Schaerer, & Maselli (2006), who modelled Ly $\alpha$  radiative transfer in collapsing proto-galaxies and high-redshift galaxies respectively. In many instances we make similar assumptions as these authors, but our code was developed independently.

The paper is structured as follows. In Section 2 we give a brief summary of the salient features of our Monte-Carlo code for Ly $\alpha$  radiative transfer and show results for standard test problems. In Section 3 we discuss our assumptions for the distribution and the physical properties of the gas. We also show the dependence of the surface brightness profile and the spectral line shapes on these assumptions. In Section 4 we present the results for a consistent model of the size distribution and the luminosity function of the faint Ly $\alpha$  emitters. The technical details of the implementation of Ly $\alpha$  radiative transfer Monte-Carlo algorithm are described in an appendix.

## 2 THE MONTE-CARLO RADIATIVE TRANSFER CODE

### 2.1 General properties of the code

Ly $\alpha$  is a resonant transition in hydrogen. The optical depth at line centre  $\tau_0$  of a typical HI region is thus generally very large. Ly $\alpha$  photons, which are expected to be produced copiously in star-forming galaxies, will therefore undergo many scatterings. Escape from the HI region usually requires diffusion in both frequency and space.

The properties of the emergent radiation depend sensitively on not only the spatial distribution of the gas, but also on its kinematics, ionization state, temperature and dust content. With modern computers Monte-Carlo sampling of the diffusion process has become the method of choice. We employ such a code for simple spatial and kinematical configurations.

Our code makes a number of well-tested assumptions and approximations. Throughout, we will use a dimensionless frequency variable  $x$ , the frequency displacement from line centre in units of the Doppler frequency width (see appendix A for details). As the photons experience a large

number of scatterings before they escape, we can inject all our photons at line centre in the fluid frame of the gas ( $x_{\text{initial}} = 0$ ) for simplicity. The photon scattering is partially coherent — in the rest frame of the scattering atom, the final frequency of the photon differs from the initial frequency only by the (often negligible) effect of atomic recoil. The direction of the photon post-scattering is chosen from a dipole distribution, although choosing an isotropic distribution makes little difference. We also incorporate a cosmic abundance of deuterium (see DHS06). Finally, we give all results in the rest frame of the centre of mass of the emitter.

Monte Carlo Ly $\alpha$  RT codes like the one used here can be significantly accelerated by skipping scatterings in the core of the line-profile [Ahn, Lee, & Lee (2002), DHS06]. In the Doppler core, the optical depth is so large that the photon experiences very little spatial diffusion while it awaits an encounter with a rapidly moving atom that will scatter it in frequency space into the wings of the line profile. The gas distributions we consider here are spherically symmetric. We exploit this symmetry by using an arrangement of spherical shells.

A detailed description of the implementation and relevant formulae of our code can be found in Appendix A.

### 2.2 Testing the code

There are a number of analytical solutions to Ly $\alpha$  radiative transfer problems against which we have tested our code.

Hummer (1962) calculated the redistribution function for the case of coherent scattering in the atom's frame with radiation damping (i.e. incorporating the Lorentzian natural line width). The result (Equation 3.12.2 of Hummer (1962)) is  $R_{\text{II-B}}(x, x') dx'$ , which is defined as the probability that a photon, whose frequency prior to absorption was  $x$ , is re-emitted with frequency in the range  $[x', x' + dx']$ . In the top left panel of Figure 1 we compare the analytic formula with the output of our code. The thin, smooth line is the analytic solution and the thick histogram is the output from our code for  $x = 0, 2, 5$  (blue, red, black respectively) for  $T = 10$  K ( $a = 0.0149$ ). The two lines are almost indistinguishable.

Harrington (1973) and Neufeld (1990) derived an analytic expression for the spectrum  $J(x, \tau_0)$  of radiation emerging from an optically thick ( $\sqrt{\pi}\tau_0 \gtrsim 10^3/a$ ), uniform, static slab of neutral hydrogen, where line-centre photons are injected at the centre of the slab, atomic recoil is neglected and  $\tau_0$  is the line-centre, centre-to-edge optical depth. The solution normalised to  $(4\pi)^{-1}$  is given by,

$$J(x, \tau_0) = \frac{\sqrt{6}}{24\sqrt{\pi}} \frac{x^2}{a\tau_0} \frac{1}{\cosh \left[ \frac{\sqrt{\pi^3/54}}{\sqrt{a\tau_0}} |x^3| \right]}. \quad (1)$$

The comparison of our code with this analytic solution is shown for  $T = 10$  K in the top right panel of Figure 1. The agreement is again very good, especially as  $\tau_0$  increases.

Next we compare the results of our code to the analogue of the above solution for a uniform, static sphere (DHS06, Equation (9)). As the bottom left panel of Figure 1 shows, the agreement is also very good.

To test the code for the case of bulk motions in the gas, we compare our code with the modelling of Loeb & Rybicki (1999). Loeb & Rybicki investigated Ly $\alpha$  RT for a uniform HI distribution undergoing Hubble expansion with

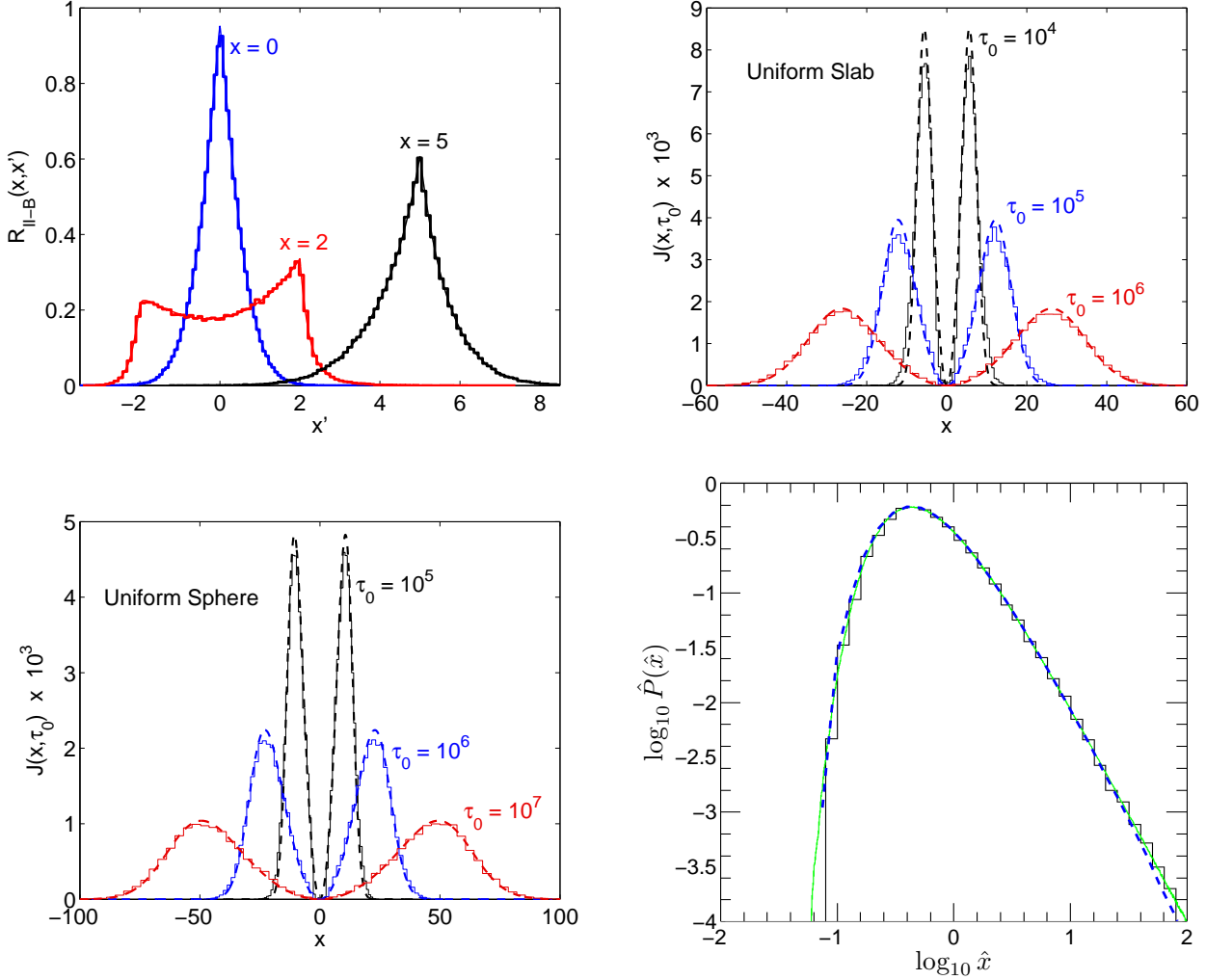


**Figure 1.** Four tests of our Ly $\alpha$  RT code. *Top left panel:* The redistribution function  $R_{\text{II-B}}(x, x')$  gives the probability that a photon, whose frequency prior to absorption was  $x$ , is re-emitted with frequency in the range  $[x', x' + dx']$ . The thin, smooth curve is the analytic solution and the thick histogram is the output from our code for  $x = 0, 2, 5$  (blue, red, black respectively), and  $T = 10$  K ( $a = 0.0149$ ). The analytic solution and our Monte-Carlo results are almost indistinguishable. *Top right panel:* For an optically thick ( $\sqrt{\pi}\tau_0 \gtrsim 10^3/a$ ), uniform, static slab of neutral hydrogen, where line-centre photons are injected at the centre of the slab, we can compare with the analytic solution of Harrington (1973) and Neufeld (1990). We set  $T = 10$  K, and  $\tau_0$  is the line-centre, centre-to-edge optical depth as labeled on the plot. The solid histogram from our code agrees again well with the analytical solution, especially as  $\tau_0$  increases. *Bottom left panel:* As above, but for a uniform sphere. The agreement is very good. *Bottom right panel:* Ly $\alpha$  RT through uniform H I undergoing Hubble expansion with velocity  $\mathbf{v}_b = H(z)\mathbf{r}$ . The histogram is the result from the code of DHS06, the green solid curve is the solution of by LR99 Loeb & Rybicki (1999), and the dashed blue line is the result of our code. The agreement is again excellent.

$\mathbf{v}_b = H(z)\mathbf{r}$ , where  $H(z)$  is the Hubble constant at redshift  $z$ . For photons blueward of line-centre in the fluid frame, the expansion of the universe will eventually redshift the photon back into resonance. Only photons redward of line centre can propagate to infinity. The optical depth to infinity is

$$\tau_\infty(\bar{x}) = -\frac{n_{\text{HI}} \sigma_0 a v_{\text{th}}}{\sqrt{\pi} H(z) \bar{x}} \equiv \frac{x_*}{\bar{x}}, \quad (2)$$

where  $\bar{x}$  is the frequency in the fluid frame. This defines a critical frequency  $x_*$ . Photons with  $\bar{x} \ll x_*$  are redshifted enough to stream freely. We follow here Loeb & Rybicki (1999) and use a new frequency variable  $\hat{x} = \bar{x}/x_*$ . We refer the reader to Appendix B2 of DHS06 for a careful discussion of the modifications necessary to permit a meaningful comparison between the two codes.

In the bottom right panel of Figure 1 we compare the results of our code with those of Loeb & Rybicki (1999), and DHS06. The relevant parameters are:  $z = 10$ ,  $n_{\text{HI}} = 2 \times 10^{-7}(1+z)^3 \text{ cm}^{-3}$  and  $T = 10\text{K}$ . Note that  $\int \hat{P}(\hat{x}) d\hat{x} = 1$ . The agreement is again excellent.

### 3 Ly $\alpha$ RADIATIVE TRANSFER IN DLAS / FAINT Ly $\alpha$ EMITTERS

#### 3.1 A simple spherically symmetric model for the spatial distribution and kinematics of the gas

##### 3.1.1 Observational and theoretical constraints

Our knowledge of the spatial distribution and kinematics of the neutral hydrogen in the DLAs / faint Ly $\alpha$  emitters is still somewhat limited. The statistics of the occurrence DLAs and their column density distribution give us integral constraints on the spatial distribution of the gas, while the velocity distribution of low ionization species tracing neutral hydrogen gives us some indication of the velocity range of bulk motions. The bulk motions of the gas appear to have velocities that range from a few tens of km/s to several hundred km/s (Prochaska & Wolfe 1997). The relative contribution of ordered and random motions and the role of gas inflow and galactic winds is, however, still very uncertain (Haehnelt, Steinmetz, & Rauch 1998, 2000; Razoumov et al. 2008; Pontzen et al. 2008; Tescari et al. 2009).

If the identification of the faint Ly $\alpha$  emitters as DLA host galaxies is indeed correct, then this gives us for the first time constraints on the spatial extent of the gas distribution in individual objects for a sizable (Ly $\alpha$ ) emission selected sample. While there is still significant ambiguity due to the unknown “duty cycle” for Ly $\alpha$  emission (as discussed by BH09), theoretical modelling gives us a handle on the halo masses and virial velocities expected to host the DLAs / faint Ly $\alpha$  emitters. By duty cycle, we mean the fraction of DM host haloes detectable through their Ly $\alpha$  emission at any given time. There are a number of reasons why this fraction may be smaller than unity. The haloes, for example, may not continuously form stars, but geometrical factors due to a preferential escape of the Ly $\alpha$  emission in certain directions due to variations in the neutral hydrogen column density (and/or the dust column density) should also contribute (Laursen, Razoumov, & Sommer-Larsen 2009; Laursen, Sommer-Larsen, & Andersen 2009).

Given these uncertainties, we have decided to follow DHS06 and investigate Ly $\alpha$  radiative transfer for sources at the centre of DM halos with a range of masses, a duty cycle for Ly $\alpha$  emission, a simple spherically symmetric gas distributions without dust, and either inflow or outflow with velocities which vary as a power law with radius. This already leads to a rich variety in the predicted surface brightness profiles and spectral shapes and allows us to study the influence of important physical parameters.

##### 3.1.2 The assumed radial distribution of neutral hydrogen

We begin by specifying the radial distribution of neutral hydrogen in a given halo. The total amount of hydrogen is set relative to the cosmic<sup>1</sup> mass fraction of hydrogen  $f_H = \Omega_H/\Omega_m$ . Throughout we assume a helium fraction of  $Y_p = 0.24$ . There are a number of reasons to suspect that the hydrogen mass fraction in a typical halo is lower than  $f_H$ .

Firstly, baryons are subject to the smoothing effects of gas pressure. Secondly, gas that forms stars is both ionised and extremely compact. Stars will also ionise the neutral gas around them — this is a source of Ly $\alpha$  but also reduces the amount of H I that remains to scatter photons. Finally, stellar and AGN driven galactic winds are expected to drive gas out of galaxies back into the IGM. As a first attempt at modelling this effect, we reduce the total mass of baryons in the halo to a fraction  $f_e$  of the cosmic value.

On top of reducing the amount of neutral hydrogen in a typical halo, it is known that the UV background will significantly ionise the gas in halos too small to self-shield. It is also easier for galactic winds to drive gas out of small, shallow halos. In BH09, this effect was implemented via an exponential suppression of the cross-section of neutral hydrogen below a critical circular velocity  $v_{c,0}$ . This was necessary in order to fit the observed velocity width distribution of associated low ionization metal absorption. Here, we will implement this suppression by reducing the total amount of neutral hydrogen in halos below  $v_{c,0}$ , such that the total mass of neutral hydrogen in a halo of mass  $M_V$  is

$$M_{H\text{I}} = f_e f_H \exp\left(-\left(\frac{v_{c,0}}{v_c}\right)^{\alpha_e}\right) M_V \quad (3)$$

(see BH09 for a detailed discussion). We use the fiducial parameters  $\alpha_e = 3$ ,  $v_{c,0} = 50 \text{ km s}^{-1}$ .

For the radial distribution of the gas, we assume an NFW profile at  $z = 3$ , characterised by a scale radius  $r_s$  defined in Navarro, Frenk, & White (1996). Following the simulations of Maller & Bullock (2004, Equation (9)), we alter the NFW profile to give the halo a thermal core at  $\simeq 3r_s/4$ . The profile is then specified by the total mass of the halo  $M_V$  and the concentration parameter  $c_v \equiv r_v/r_s$ . For dependence of the concentration parameter on the mass, we take the mean value of the  $c_v - M_V$  correlation as given by Macciò et al. (2007),

$$c_v = c_0 \left(\frac{M_V}{10^{11} M_\odot}\right)^{-0.109} \left(\frac{1+z}{4}\right)^{-1}. \quad (4)$$

For dark matter, Macciò et al. (2007) found that  $c_0 \approx 3.5$ , with a log-normal distribution and a scatter around this mean value of  $\Delta(\ln c_v) = 0.33$ , in agreement of the results of Bullock et al. (2001) and Wechsler et al. (2002). As we will find later, a significantly larger  $c_0$  is appropriate for the baryons; we will use the column density distribution of DLAs to constrain  $c_0$  in Section 4.2. As we discuss further in Section 4.5, the gas in the DLAs / faint emitters can be expected to self-shield against the meta-galactic ionizing UV background at  $z \sim 3$ . The corresponding self-shielding radius in the DM halos we are studying here is generally smaller than the virial radius. We therefore set the outer radius of the H I to be the virial radius in our modelling and also ignore radiative transfer through the IGM. We set  $T = 10^4 \text{ K}$  as a fiducial temperature.

##### 3.1.3 The assumed kinematics of neutral hydrogen

The biggest uncertainty in our modelling is probably the kinematical state of the gas. We follow DHS06 and for our fiducial model we assume the gas to be infalling with a

<sup>1</sup> The relevant cosmological parameters used in this work are:  $(h, \Omega_M, \Omega_b, \Omega_\Lambda, \sigma_8, n) = (0.7, 0.3, 0.045, 0.7, 0.9, 1)$ .

power-law radial velocity profile<sup>2</sup> parameterised by  $v_{\text{amp}}$  and  $\alpha$

$$v_{\text{bulk}}(\mathbf{r}) = -v_{\text{amp}} \left( \frac{r}{r_v} \right)^\alpha \hat{\mathbf{r}} \quad (5)$$

where  $r_v$  is the virial radius, for which we follow the definition of Maller & Bullock (2004). Values in the range  $\alpha \in [-0.5, 1]$  should be reasonable. The upper limit describes a spherical top-hat collapse, while the lower limit represents the accretion of massless shells onto a point mass ( $v^2 \sim GM/r$ ). A spherical top-hat would have  $v_{\text{amp}} = v_c$ .

While gas infall will certainly be an important feature of the gas kinematics, star formation driven outflows are also likely to play a role (see Veilleux, Cecil, & Bland-Hawthorn 2005, for a review). Note that for a spherically symmetric gas distribution, the red and blue side of the line profiles will just be interchanged if the gas is assumed to be outflowing instead of inflowing with the same velocity profile (ignoring the very slight effects of recoil and deuterium). For the more massive and more actively star-forming LBGs, galactic winds have been suggested to sweep up an expanding shell (Pettini et al. 2000, 2002; Verhamme, Schaerer, & Maselli 2006; Schaerer & Verhamme 2008; Verhamme et al. 2008; Quider et al. 2009). We investigate such a configuration in Section 3.3.

### 3.1.4 The fiducial model

R08 and BH09 identified star-formation as the most likely source for the faint emitters. Wolfe & Chen (2006) used continuum emission to place stringent limits on *extended* star formation in DLAs. We have thus assumed a centrally-peaked emissivity — all photons are created at  $\mathbf{r} = \mathbf{0}$ .

Before we attempt to model the data of R08 in detail, we will consider the effect on the spectra and surface brightness distribution of altering the parameters of our model. Our fiducial model parameters are  $(z, M_v, c_0, f_e, v_{\text{amp}}, T) = (3, 10^{11} M_\odot, 25.3, 0.2, v_c, 10^4 \text{K})$ . The values of  $c_0$  and  $f_e$  that we have chosen will be justified in Section 4.2. The surface brightness  $S$  scales with the total luminosity  $L_{\text{Ly}\alpha}$ , which will be given in the caption to each figure. The values of the luminosity chosen will be justified in section 4.3. The velocity and column density profiles for the fiducial model are shown in Figure 2, where the column density is as seen along a sightline that passes all the way through the halo at an impact parameter  $y$ .

## 3.2 Ly $\alpha$ radiative transfer in individual halos with gas infall

In this section, we will consider the effects of changing the most important parameters in the model: mass, concentration, velocity profile (parameterized by the power law index  $\alpha$ ) and baryon fraction. Further parameters (temperature and amplitude of the bulk motions of the gas) are discussed in Appendix B.

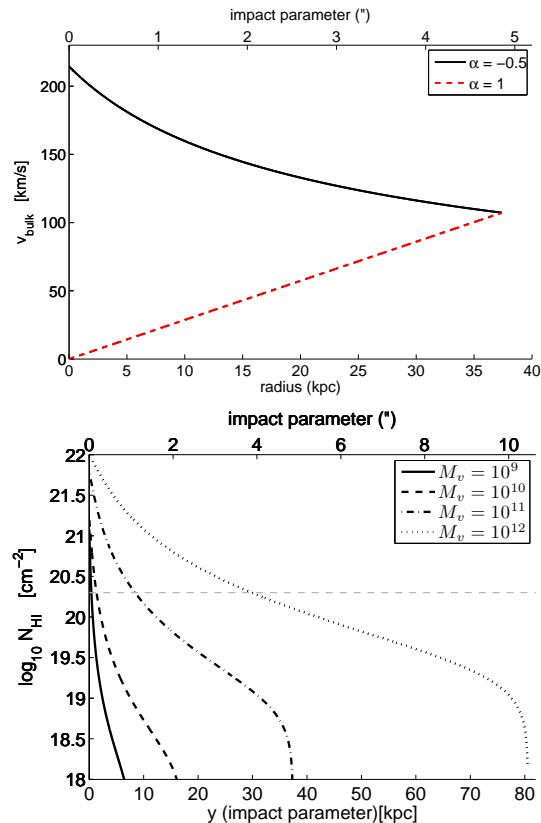


**Figure 2.** *Top:* The velocity profile for the fiducial halo, for differing values of  $\alpha$  as shown in the legend. *Bottom:* The column density profiles for the fiducial model with the total mass as given in the legend in units of  $M_\odot$ . The column density is calculated along a sightline that passes all the way through the halo at a distance  $r$  from its centre. Note that the  $10^9 M_\odot$  line has been boosted by a factor of  $10^4$  to make it visible on the given axes. The horizontal dashed line indicates the minimum column density of a DLA.

### 3.2.1 The effect of halo mass and concentration

The models of BH09 give us a handle on the masses of the halos that host DLAs. Figure 3 considers halos with masses of  $M_v = 10^9, 10^{10}, 10^{11}, 10^{12} M_\odot$ , which at  $z = 3$  correspond to  $v_c = 23, 50, 107, 231 \text{ km s}^{-1}$ ,  $r_v = 8, 17, 37, 81 \text{ kpc}$ ,  $b_{\text{max}} = 1.05, 2.25, 4.9, 10.5 \text{ arcsec}$ , where  $b_{\text{max}}$  is the angular radius corresponding to  $r_v$ .

We see that, as the mass increases, the emerging photons emerge bluer. This is because, as we add more gas, the central column densities increase and the photons must shift further from line centre in order to escape. The  $\alpha = 1$  profiles are increasingly double-peaked for lower masses, while the  $\alpha = -0.5$  profiles only ever have one, blue peak. This is because the innermost region of the  $\alpha = 1$  halo has the smallest bulk velocity, and thus most resembles the uniform, static sphere of Figure 1. As the bulk velocities increase at the centre of the halo, the amount of energy transferred between the gas and photons in each scattering is increased, favouring one of the two peaks (the blue/red peak for inflowing/outflowing gas respectively).

The surface brightness profile shows that the dominant effect in increasing the mass is that the virial radius (which we have assumed to be the outer radius of the H I) increases.

<sup>2</sup> We use the modification to this law for  $\alpha < 0$  given in Equation 10 of DHS06.

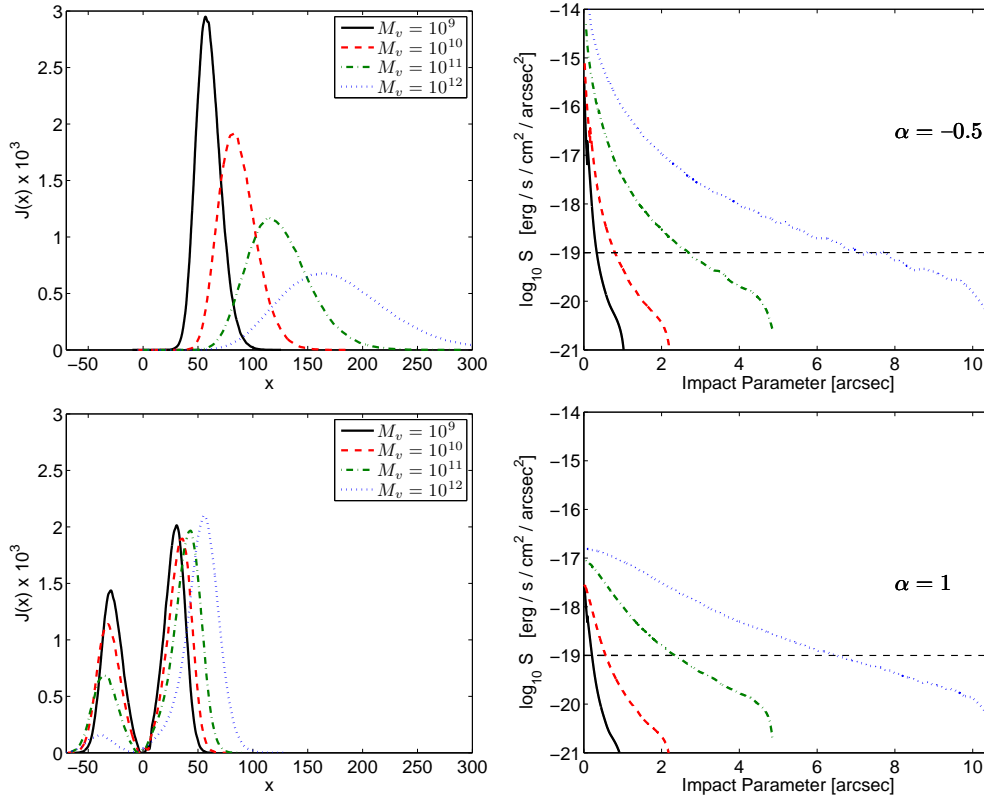


**Figure 3.** Spectra (left panels) and surface brightness profiles (right panels) for emission in halos with total mass as given in the legend in units of  $M_\odot$ . The top panels are for  $\alpha = -0.5$ , with a total  $\text{Ly}\alpha$  luminosity which scales with the mass of the DM halo as required to fit the observed luminosity function in Fig. 10 (see section 4 for more details). In the order given in the legend the luminosities are  $L_{\text{Ly}\alpha} = (9.6 \times 10^{-6}, 0.88, 22, 240) \times 10^{42} \text{ erg s}^{-1}$ . The bottom panels are for  $\alpha = 1$ , with  $L_{\text{Ly}\alpha} = (4.8 \times 10^{-7}, 0.044, 1.1, 12.1) \times 10^{42} \text{ erg s}^{-1}$ . Note that the surface brightness for the  $M = 10^9 M_\odot$  model has been raised by a factor  $10^4$  to be able to plot it in the same plotting window. As the mass increases, the emerging photons emerge bluer, and are scattered to larger radii in the larger halos. The dashed horizontal line is the detection threshold of the Rauch et al. emitters.

The  $\alpha = -0.5$  profile is much more centrally peaked than the  $\alpha = 1$  profile. The reason is that the larger bulk velocities at the centre of the  $\alpha = -0.5$  halo can shift the photon into the wings of the spectral line, resulting in reduced spatial diffusion.

For the concentration parameter, we have considered the values 1.8, 3.5, 9.4 and 25.3. The spectra and surface brightness profiles for these models are shown in Figure 4.

As the concentration increases, the photons generally emerge bluer. The  $\alpha = 1$  profile becomes *more* double-peaked as the concentration increases, because the HI column density increases at smaller radii, where the bulk velocity is lower. The surface brightness profile is also more centrally peaked for higher concentrations, as more scatterings occur at smaller radii.

### 3.2.2 The effect of baryonic fraction/column density

The effect of changing the baryonic fraction  $f_e$  is shown in Figure 5. As baryons are removed from the halo, the spectrum shifts toward  $x = 0$  and the surface brightness profile becomes more centrally peaked, as there is less gas in the outer parts of the halo to scatter the photons. The baryon fraction where the photons are not scattered efficiently anymore to the virial radius (where we have the gas distribution assumed to cut-off) corresponds to a HI column density<sup>3</sup> of about  $10^{16} \text{ cm}^{-2}$ . For very small  $f_e$  and  $\alpha = -0.5$ , some of the photons can escape the halo without scattering at all,

creating a very narrow peak at  $x = 0$ . Some of the spectra also show a trough at  $x \approx 6$  due to deuterium. Note, however, that for  $f_e \ll 0.1$  the gas in the halos would not be able to self-shield anymore against the meta-galactic UV background at  $z \sim 3$  so the model would be internally inconsistent for such small baryonic fractions.

### 3.3 Expanding Shells

For the much brighter  $\text{Ly}\alpha$  emission seen in many LBGs, the  $\text{Ly}\alpha$  emission is systematically red-shifted by several hundred  $\text{km s}^{-1}$ . This is generally attributed to backscattering of the  $\text{Ly}\alpha$  radiation from a wind-driven expanding shell. Verhamme, Schaerer, & Maselli (2006) used a  $\text{Ly}\alpha$  RT code similar to ours to calculate the emergent spectrum from an expanding shell. We will investigate here in a similar fashion if this picture could apply to the R08 emitters. We consider a shell of HI, where the inner radius is a fraction  $f_r$  times the outer radius  $r_{\text{max}}$ . The shell is expanding at a uniform velocity  $V_{\text{exp}}$ , and has a column density of  $N_{\text{HI}}$ . The temperature is set by the Doppler velocity<sup>4</sup>  $b_T$ . Our fiducial model has the parameters:  $(r_{\text{max}}, f_r, V_{\text{exp}}, N_{\text{HI}}, b_T) = (30 \text{ kpc}, 0.9, 300 \text{ km s}^{-1}, 2 \times 10^{20} \text{ cm}^{-2}, 40 \text{ km s}^{-1})$ , similarly to the fiducial model of Verhamme et al. For the outer radius of the shell  $r_{\text{max}}$  we have chosen a value similar to the models of the previous sections.

Figure 6 shows the effect of altering the parameters that Verhamme et al. found to be most important, the column

<sup>3</sup> Which is somewhat dependent on the spatial profile of neutral hydrogen and the velocity field.

<sup>4</sup> This is defined in the same way as the thermal velocity dispersion (in the Appendix), with a possible contribution from a turbulent velocity dispersion, added in quadrature.

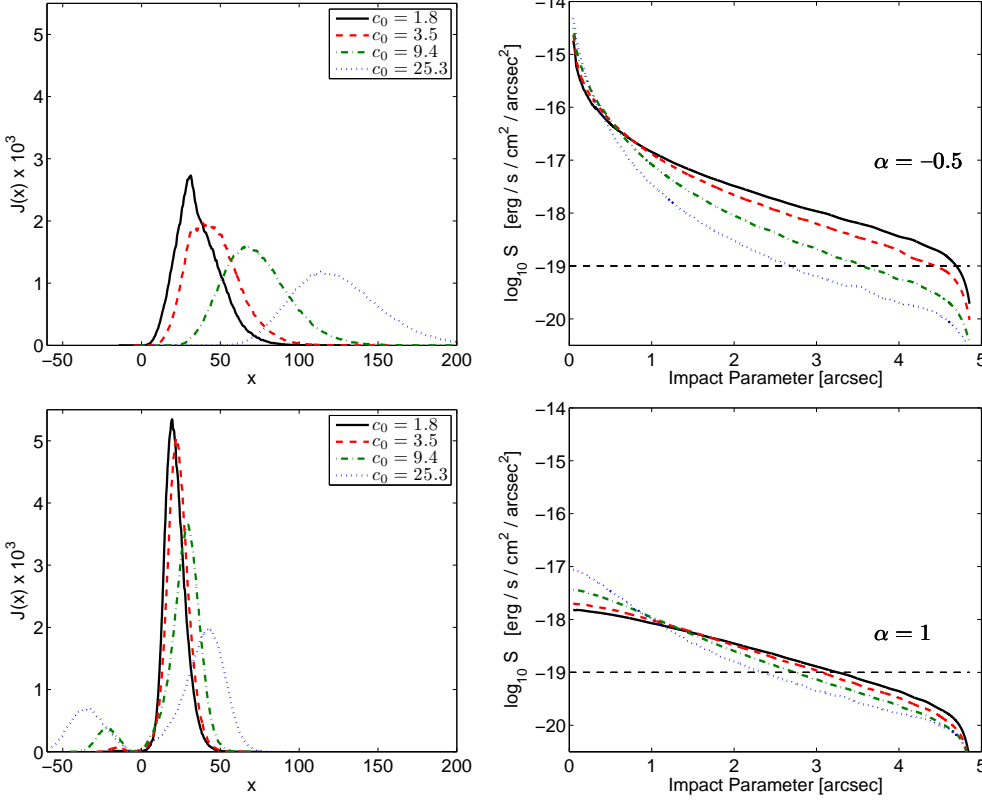


**Figure 4.** Spectra and surface brightness profiles for emission in halos with concentration parameter  $c_0$  as given in the legend. The top panels are for  $\alpha = -0.5$ , for which  $L_{\text{Ly}\alpha} = 2.2 \times 10^{43} \text{ erg s}^{-1}$ . The bottom panels are for  $\alpha = 1$ , for which  $L_{\text{Ly}\alpha} = 1.1 \times 10^{42} \text{ erg s}^{-1}$ . As the baryon distribution becomes more centrally concentrated, the photons emerge bluer. The photons are scattered at larger radii in the less concentrated halos. The dashed horizontal line is the detection threshold of the Rauch et al. emitters.

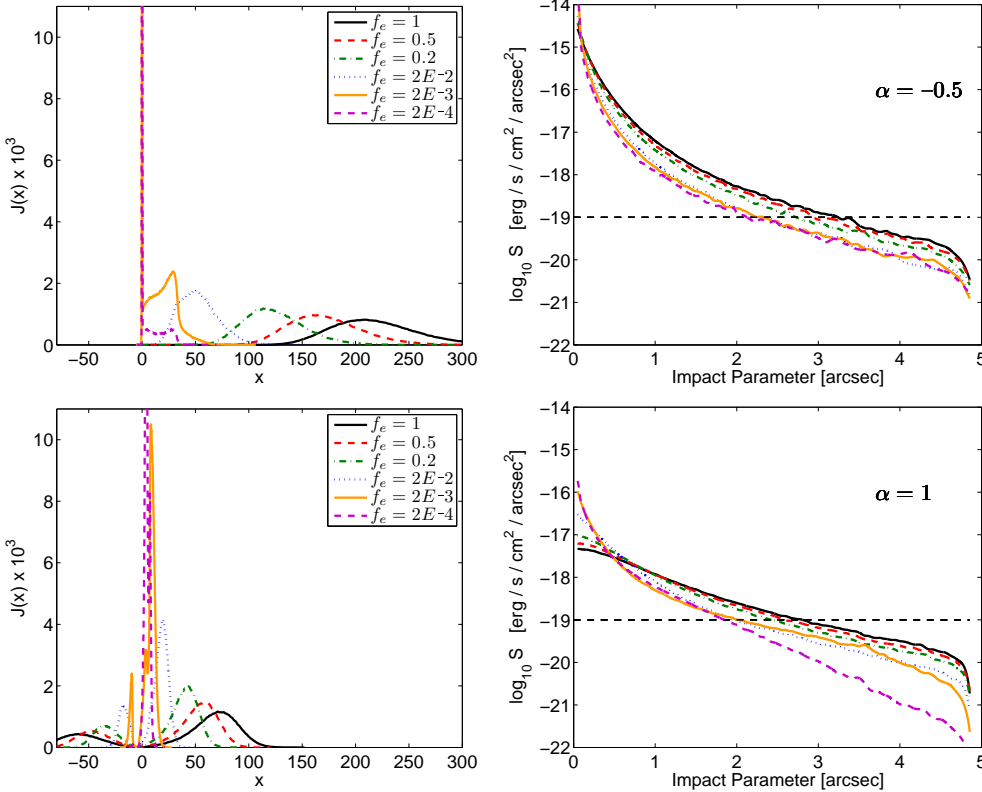


**Figure 5.** Spectra and surface brightness profiles for emission in halos with baryon fraction  $f_e$  as given in the legend, where  $f_e = 1$  corresponds to the cosmic value of the baryon fraction. The top panels are for  $\alpha = -0.5$ , the total luminosity is kept the same for each model at  $L_{\text{Ly}\alpha} = 2.2 \times 10^{43} \text{ erg s}^{-1}$ . The bottom panels are for  $\alpha = 1$ , with  $L_{\text{Ly}\alpha} = 1.1 \times 10^{42} \text{ erg s}^{-1}$ . As  $f_e$  decreases, the spectral shift decreases and the surface brightness becomes more centrally peaked. The dashed horizontal line is the detection threshold of the Rauch et al. emitters.



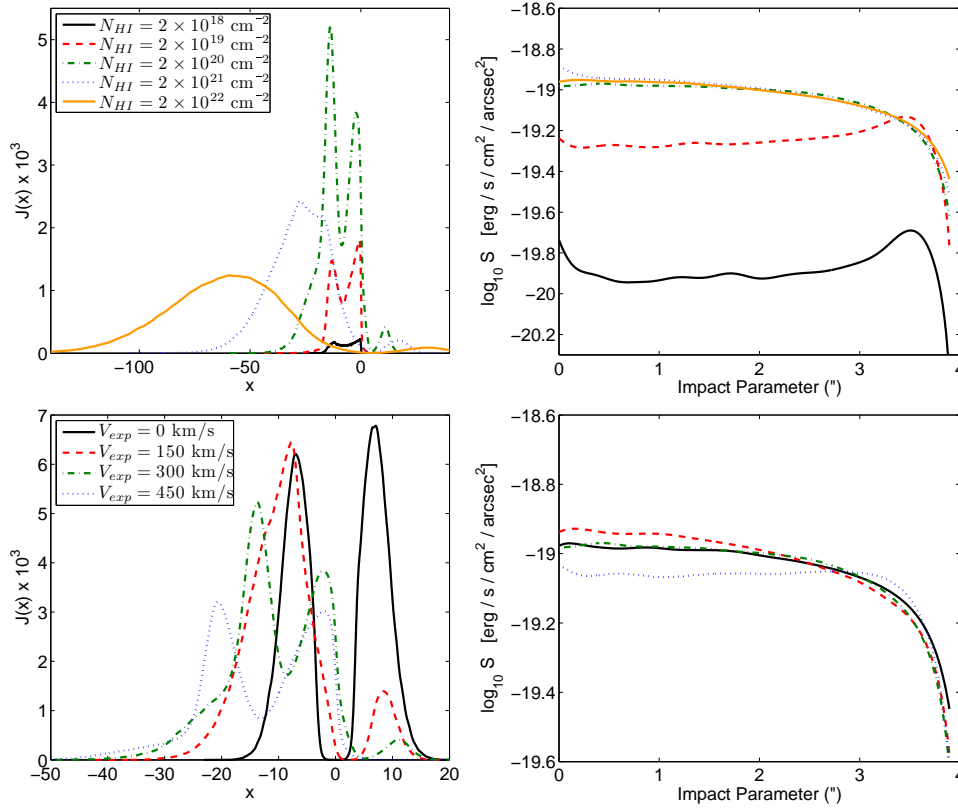


**Figure 6.** Spectra and surface brightness profiles for the modelling of expanding shells. The panels show the effect of altering the parameters that Verhamme et al. found to be most important, the column density and the expansion velocity, as given in the legend. Note that, for small column densities (in the upper panels), a certain fraction of photons were able to escape directly without scattering. These photons form a delta function at  $x = 0$ , and at small impact parameter, which has been removed from these plots for clarity. As the column density increases (top panels), the spectrum becomes redder, and the small blue peak disappears. The most significant change in the surface brightness profile comes at small column densities as photons are able to escape directly, leaving less to be scattered at large radii. As the expansion velocity increases (bottom panels), the back-scattering mechanism becomes more pronounced, creating the two red peaks. At small velocities, the results become similar to that for a static sphere.

density and the expansion velocity. Note that, for small column densities (upper panels), a certain fraction of photons were able to escape directly without scattering. These photons form a very sharp peak at  $x = 0$ , and at small impact parameter, which has been removed from these plots for clarity.

As the column density increases (top panels), the spectrum becomes redder, and the small blue peak disappears, as the photons must scatter further from line centre in order to escape. The most significant change in the surface brightness profile occurs for small column densities, where some of the photons are able to escape directly, leaving fewer to scatter at large radii.

As the expansion velocity increases (bottom panels), the back-scattering mechanism becomes more pronounced. Photons which scatter off the far side of the shell back through its interior are far enough from line centre to escape through the front side of the shell. This mechanism creates the two red peaks (the reddest peak comes from photons that backscatter more than once). At small velocities, we approach a profile similar to the static sphere.

The surface brightness profiles are very flat when compared to the infall/outflow models of the gas in an NFW halo which we had considered before. Qualitatively, they appear much flatter than the profiles of the R08 emitters. Almost all of the R08 emitters show a central peak. One way to produce a central peak for a shell geometry is for the column density to be low enough for photons to be able to escape directly; the resolution of the instrument then broadens the delta function at  $y = 0$  into a central peak. This would limit the column density of the shell to  $N_{\text{HI}} \lesssim 2 \times 10^{19} \text{ cm}^{-2}$ . We

conclude that the R08 emitters appear unlikely to be halo-scale expanding shells of HI around a central Ly $\alpha$  source.

### 3.4 Summary of general trends of the Ly $\alpha$ emission

The radial (column) density distribution and the velocity field are the physical properties which most strongly affect the spectral distribution of the Ly $\alpha$  emission in our modelling. For a spherical density distribution with neither outflow nor infall, the distance between the peaks increases with increasing optical depth in the same way as the uniform static slab solution. Infall and outflow lead to a suppression of the red/blue peak and an increased shift of the opposite peak. The suppression increases with increasing velocity amplitude and optical depth.

The surface brightness profile depends strongly on the radial velocity profile. With increasing amplitude of the bulk motion, the diffusion in frequency space is accelerated and the emission becomes more centrally peaked. In our model with increasing amplitude towards decreasing radius ( $\alpha = -0.5$ ), the average bulk motions are larger and the effect is more pronounced. In the model with the expanding shell, the photons can travel unimpeded until they encounter the shell which leads to a rather flat surface brightness profile.

The photons diffuse radially until the column density of neutral hydrogen density drops to values around  $10^{16} \text{ cm}^{-2}$  somewhat dependent on the spatial profile of neutral hydrogen and the velocity field. The faint extended Ly $\alpha$  emission should thus have a rather sharp edge which is defined by the surface inside which the gas is able to self-shield and the optical depth rises rapidly.



## 4 MODELLING THE RAUCH ET AL. EMITTERS

### 4.1 Surface brightness profiles and spectral shapes

We begin with a qualitative summary of the properties of the R08 emitters. Note, however, that due to the faintness of the sources the spectral and spatial profiles are rather noisy, making it difficult to identify signatures of inflow (more prominent blue peak) or outflow (more prominent red peak)<sup>5</sup>. As discussed in R08, for 12 of the 27 spectra only a single emission peak is visible while six/three of the spectra show a weak secondary blue/red counter-peak. The remaining spectra are extended in frequency space without a clear peak structure. The widths of the spectral peaks ranges from  $\sim 250 - 1000 \text{ km s}^{-1}$ , which corresponds to  $\Delta x \sim 20 - 80$  for gas with a temperature of  $10^4 \text{ K}$ . The surface brightness profiles are predominantly centrally peaked with wings that often extend well beyond the Gaussian core of the PSF. This is particularly true of the brightest sources, while the fainter sources are more difficult to characterise due to the noise.

### 4.2 Simultaneous modelling of DLA properties

Modelling the radial distribution of neutral hydrogen in DM halos allows us to calculate the column density distribution along sightlines that intersect the halos. Comparison with the observed column distribution of DLAs provides a useful constraint in this regard. We will use here the same notation as BH09.

The column density distribution is defined such that the number of systems ( $d^2\mathcal{N}$ ) intersected by a random line of sight between absorption distance<sup>6</sup>  $X$  and  $X + dX$ , with HI column density between  $N_{\text{HI}}$  and  $N_{\text{HI}} + dN_{\text{HI}}$  is,

$$d^2\mathcal{N} = f(N, X) dX dN_{\text{HI}}. \quad (7)$$

For our model we calculate this quantity using the Press-Schechter formalism. We need two ingredients. The first is  $n_M(M, X)$ , the mass function of dark matter halos, as calculated by Sheth & Tormen (2002). The second ingredient is the column density of neutral hydrogen in a given halo (of mass  $M$  at absorption distance  $X$ ), as a function of the (physical) impact parameter  $y$ ,  $N_{\text{HI}}(y|M, X)$ . This is calculated from the neutral hydrogen density as a function of radius. Given that  $N_{\text{HI}}$  is a monotonically decreasing (and thus invertible) function of  $y$ , the region between  $N_{\text{HI}}$  and  $N_{\text{HI}} + dN_{\text{HI}}$  is an annulus with cross-sectional area  $d(\pi y^2)$ . Hence, we can write the column density distribution as,

$$f(N, X) = \frac{c}{H_0} \int n_M(M, X) \left| \frac{d(\pi y^2)}{dN_{\text{HI}}} (N_{\text{HI}}|M, X) \right| dM. \quad (8)$$

The results are shown in Figure 7. The most important parameters (given that we integrate over all  $M$ ) are the normalisation of the concentration parameter for the baryons  $c_0$ , and the baryon fraction  $f_e$  relative to the cosmic value.

<sup>5</sup> Recall also that this can be more complicated for the case of an outflowing shell, as there are then two red peaks.

<sup>6</sup> The absorption distance is defined by

$$dX \equiv \frac{H_0}{H(z)} (1+z)^2 dz. \quad (6)$$

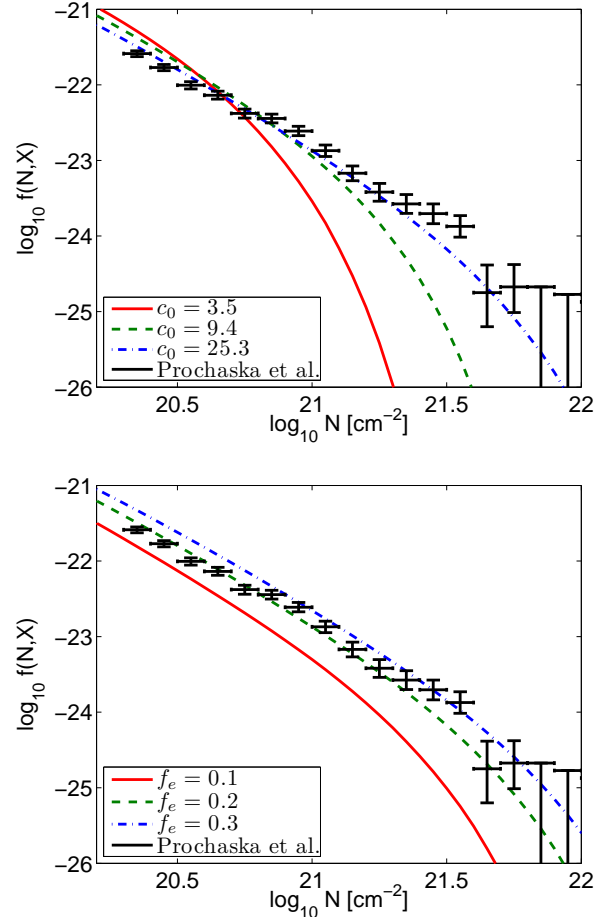


**Figure 7.** The column density distribution  $f(N, X)$  for our model; the black crosses show the data of Prochaska & Wolfe (2009). The upper panel shows the effect of changing the concentration parameter of the radial gas density profiles. The lower panel shows the effect of altering the baryon fraction  $f_e$  (defined relative to the cosmic value).

A good fit to the observed column density distribution is obtained for  $c_0 \approx 25.3$  and  $f_e \approx 0.2$ . The figure demonstrates the effect of altering these two parameters. Decreasing  $f_e$  decreases the overall normalisation, while  $c_0$  mostly affects the high column density end of the distribution. Changing  $v_{c,0}$  has a comparatively small effect.

Note that our model somewhat overpredicts the number of absorption systems with column densities below  $N_{\text{HI}} = 20.3 \text{ cm}^{-2}$ , in the regime of Lyman Limit systems (LLs). In this column density range the observed  $f(N, X)$  flattens significantly (O’Meara et al. 2007), an effect which can be attributed to the inability of (super) LLs to self-shield completely against the meta-galactic UV background (Zheng & Miralda-Escudé 2002). Since we have not attempted to model the ionization of the gas and in particular the self-shielding of the gas in any detail, it is not surprising that our model does not reproduce this. The UV background should, however, not effect our results for the population of predominantly neutral DLAs. Figure 5 shows that in the LLs regime the inferred size of the emission region depends very weakly on column density.

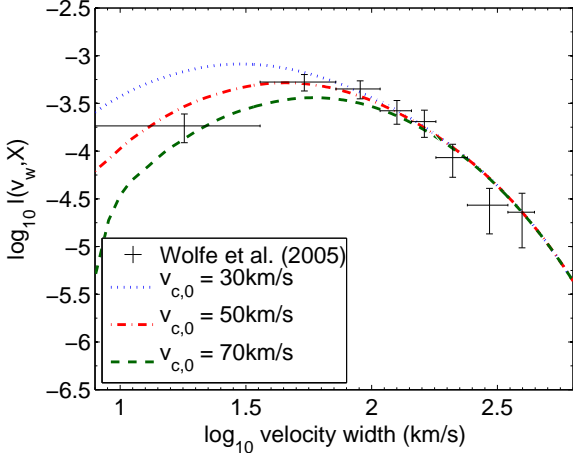


**Figure 8.** The velocity width distribution  $l(v_w, X)$  of the associated low-ionization metal absorption of DLAs. The black crosses show the observational data compiled in Figure 10 of Wolfe, Gawiser, & Prochaska (2005). The legend shows the parameter  $v_{c,0}$ , below which the baryonic fraction is assumed to be suppressed due to the effect of photo-heating and/or galactic winds.

Similarly to BH09, we can also calculate the predicted probability distribution of the velocity width  $v_w$  of the associated low ionization metal absorption of DLAs for our model as follows,

$$l(v_w, X) = \frac{c}{H_0} \int_0^\infty p(v_w|v_c(M)) n_M(M, X) \sigma_{\text{DLA}}(M, X) dM, \quad (9)$$

where  $p(v_w|v_c(M))$  is the conditional probability distribution as discussed in Section 2 of BH09. The DLA cross-section is given by  $\sigma_{\text{DLA}}(M) = \pi y_{\text{DLA}}^2$ , where  $N_{\text{HI}}(y_{\text{DLA}}|M, X) = 10^{20.3} \text{ cm}^{-2}$ . The result is shown in Figure 8, along with the observational data of Wolfe, Gawiser, & Prochaska (2005)

As in BH09 our model fits the data well with values of  $v_{c,0}$  in the range  $50 - 70 \text{ km s}^{-1}$ . We should point out that the probability distribution  $p(v_w|v_c)$  was originally derived from simulations which do not include the effect of galactic winds and where the distribution of gas in a given halo is somewhat different from what we have assumed here (see Barnes & Haehnelt (2009) for a more detailed discussion).

We should also emphasize that, rather than using a simple power-law scaling for the absorption cross section of DLAs as in BH09, we have used here a radial distribution of neutral hydrogen which is simultaneously consistent with the column density distribution of DLAs and the size distribution of the Rauch et al. emitters, as we will see in the next section.

### 4.3 The size distribution and luminosity function

We will not attempt to fit the individual rather noisy spectral and surface brightness profiles of the R08 emitters here, but we will instead focus on the statistical properties of the population of emitters.

We calculate the cross-section weighted size distribution  $dN/dz (> r)$  expected from our model as follows. The

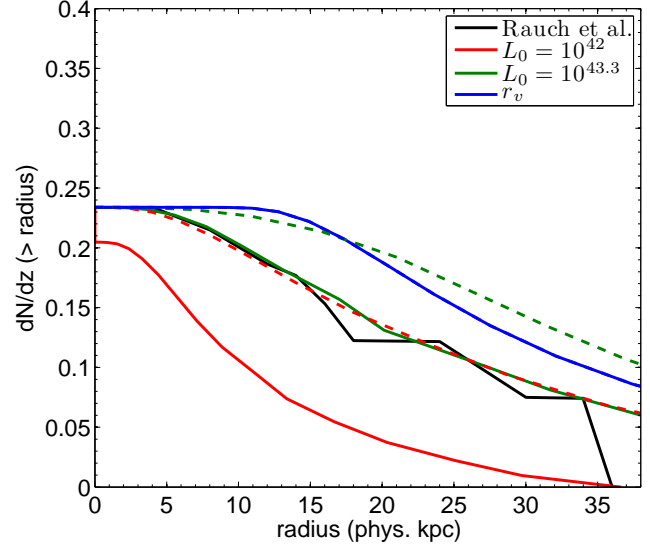


**Figure 9.** The cumulative size distribution  $dN/dz (> r)$  of the Ly $\alpha$  emitters, compared with the observations of Rauch et. al (black curve). The coloured solid curves are for  $\alpha = -0.5$ , while the dashed curves are for  $\alpha = 1$ . The red and green lines are for the  $L \propto M_{\text{HI}}$  model, with the values of  $L_0$  as given in the legend. The blue curve assumes that  $r = r_v$ , that is, assuming we can see emission all the way to the virial radius. The lines have been normalised to  $dN/dz = 0.23$  assuming a duty cycle of the Ly $\alpha$  emission with  $f_d$ , such that  $n_M^{\text{emitters}} = f_d n_M^{\text{halos}}$ . The values of  $f_d$  for each model (in the order they appear in the legend) are  $f_d = 1, \mathbf{0.2}, 0.055$  for  $\alpha = -0.5$  and  $f_d = \mathbf{0.28}, 0.07, 0.055$  for  $\alpha = 1$ . The models with the two values in bold correspond best to the data.

observations of Rauch et al. (2008) achieved a  $1 \sigma$  surface brightness detection limit of  $S_0 = 10^{-19} \text{ erg s}^{-1}$ . We calculated the expected observed size of our model emitters by determining the radius  $r$  (or equivalently, impact parameter) at which the surface brightness drops below the R08 limit,  $S(r) = S_0$ .

This procedure gives the radius of the emitter as a function of the mass of the halo. To do this, we need to specify the intrinsic Ly $\alpha$  luminosity  $L_{\text{Ly}\alpha}$  as a function of mass. Similarly to BH09, we assume that the luminosity is proportional<sup>7</sup> to the total mass of neutral hydrogen,

$$L_{\text{Ly}\alpha} = L_0 \left( \frac{M_{\text{HI}}}{2.4 \times 10^9 M_\odot} \right) \text{ erg s}^{-1}. \quad (10)$$

This means that the luminosity is subject to the same exponential suppression as the (neutral) gas content of DM halos for small circular velocities.

We now calculate the size distribution in the form of the inferred cumulative incidence rate  $dN/dz (> r)$  and compare it with the data of R08 in Figure 9. The curves have been normalised to  $dN/dz = 0.23$  by assuming the emission occurs with a duty cycle  $f_d$ ,  $n_M^{\text{emitters}} = f_d n_M^{\text{halos}}$ . The values of  $f_d$  for each model are given in the caption to the figure. The solid curves are for  $\alpha = -0.5$ , while the dashed curves are for  $\alpha = 1$ . The red and green curves assume  $L \propto M_{\text{HI}}$ ,

<sup>7</sup> The constants of proportionality are chosen to that without the suppression below  $v_{c,0}$  and with  $f_e = 0.2$ ,  $L_0$  defined below has the same value as in BH09.

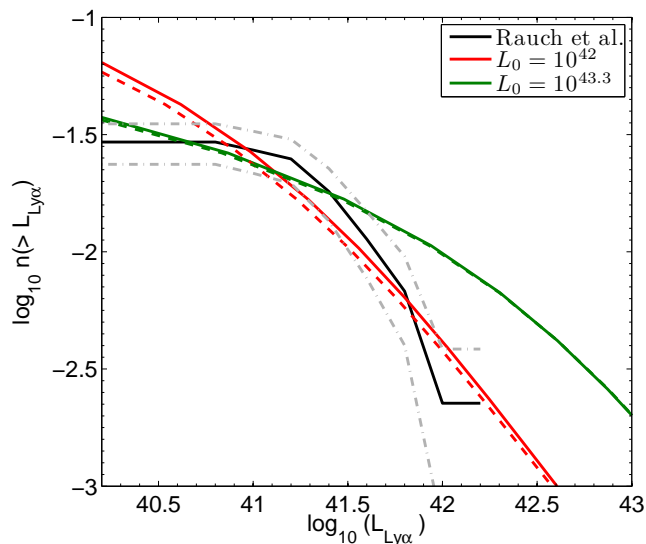


**Figure 10.** The cumulative luminosity function  $n(> L_{\text{Ly}\alpha})$  of our model, along with the Rauch et al. data (black solid curve with errors indicated by the grey dot-dashed curves). The same models are shown as in Figure 9, except that the duty cycle is chosen to match the luminosity function data. The parameters for each model (in the order they appear in the legend) are (with negligible dependence on  $\alpha$ ):  $f_d = 0.28, 0.07$ .

with the values of  $L_0$  as given in the legend. The blue curve shows the size distribution assuming that  $r = r_v$ , that is, assuming that the emission is detected all the way to the virial radius.

As we have defined the size of the emitters at a fixed flux level  $S_0$ , the observed size of the halos becomes larger as  $L_0$  increases. For  $\alpha = -0.5$  the region with emission above this flux level is smaller than in the model with  $\alpha = 1$  halos, due to the more centrally concentrated surface brightness profile. The size distribution flattens at small  $r$  due to the exponential suppression of the luminosity at low  $v_c$ .

Figure 9 shows that we can find values of  $L_0$  that fit the observed cumulative size distribution well, where the value of  $L_0$  depends on  $\alpha$ . The required duty cycle is  $\sim 20 - 28\%$ , and is fairly insensitive to  $\alpha$ . The value of  $L_0$  for  $\alpha = -0.5$  is rather high, due to the very peaked surface brightness profiles in this case.

Figure 10 shows the corresponding luminosity distribution  $n(> L_{\text{Ly}\alpha})$ , along with the R08 data (black solid curve). Note that the luminosity  $L_{\text{Ly}\alpha}$  predicted by our model is calculated by integrating the surface brightness inside the radius  $r$  where the surface brightness is above the observational limit. Photons that are scattered to radii where the surface brightness falls below this limit are lost in the noise; the observed luminosity is thus always less than the intrinsic luminosity. Note further that the observed luminosities have not been corrected for “slit losses”. The actual Ly $\alpha$  luminosities may thus be a factor two or more larger. Note finally, that the intrinsic Ly $\alpha$  emission could be significantly larger due to absorption by dust.

The figure shows the same models as in Figure 9, except that the duty cycle is chosen to fit the luminosity function data. The solid and dashed curves are very close, meaning

that there is practically no dependence on  $\alpha$ . The corresponding values of  $f_d$  are given in the caption to the figure.

The observed luminosity function is reproduced reasonably well by our model if we assume  $L_0 = 10^{42} \text{ erg s}^{-1}$ , the value required to match the observed size distribution for our model with  $\alpha = 1$ . This model predicts a somewhat steeper faint end slope than appears to be observed, but as discussed in R08 it is uncertain whether the turn-over in the observed luminosity function is real or due to incomplete identification of emitters close to the detection threshold. Should the turnover consolidate with deeper data then this may suggest a somewhat sharper cut-off of the efficiency for Ly $\alpha$  emission in shallow potential wells as we had e.g. assumed in BH09. The required duty cycle is  $f_d = 0.28$  and thus comparable to the value required to fit the observed size distribution. With  $\alpha = 1$ ,  $L_0 = 10^{42} \text{ erg s}^{-1}$ ,  $f_d \sim 0.28$  our model therefore fits both the observed size and luminosity distribution of the R08 emitters. As previously discussed, the model with  $\alpha = -0.5$  has strongly centrally peaked emission. As is apparent from Figure 10 this leads to a mismatch with the observed luminosity function if we fix  $L_0 = 10^{43.3}$  to fit the observed size distribution for this value of  $\alpha$ . Even for a significantly smaller duty cycle of  $f_d = 0.07$  we cannot match the shape of the observed luminosity function, which in this case is significantly steeper than predicted by the model over the full range of luminosities.

We therefore conclude that we can successfully reproduce both the absorption properties of DLAs and the Ly $\alpha$  emission data of R08, using a self-consistent model with centrally concentrated, star-formation powered Ly $\alpha$  production with a duty cycle of  $\sim 25\%$ , coupled with radiative transfer effects that set the observed size of the emitters *if* the velocity field of the gas facilitates the scattering of the photons to large radii with moderate central bulk velocities as in the model with  $\alpha = 1$ . Our model’s success in simultaneously reproducing the absorption properties of DLAs significantly strengthens the assertion of Rauch et al. (2008) that the faint emitters are in fact the host galaxies of DLAs.

Finally we calculate  $d^2\mathcal{N}/dX/d\log_{10} M$ , the contribution to the incidence rate from halos of different masses. The result is shown in Figure 11. The majority of DLAs/emitters have masses in the range  $10^{9.5} - 10^{12} M_\odot$  for all models. This is a similar range of masses to that found in the numerical simulations of Nagamine et al. (2007); Razoumov et al. (2008); Pontzen et al. (2008); Tescari et al. (2009). We refer the reader to BH09 for a more detailed comparison of our prediction of  $d^2\mathcal{N}/dX/d\log_{10} M$  with that of numerical simulations. The success of Pontzen et al. (2008) in reproducing the observed metallicity distribution is additional evidence in favour of this mass range, as are the observed spatial correlation of DLAs and LBGs (Cooke et al. 2006).

#### 4.4 Differences to our previous modelling

In BH09, we presented modelling in which we assumed simple scaling relations for the sizes and luminosities of the Rauch et al. emitters with the masses/circular velocities of their DM host haloes. The scaling relation for the sizes was motivated by the modelling of the velocity width distribution of the associated low ionization metal absorption of DLAs by Haehnelt, Steinmetz, & Rauch (1998). No attempt to model the spatial and spectral distribution of the

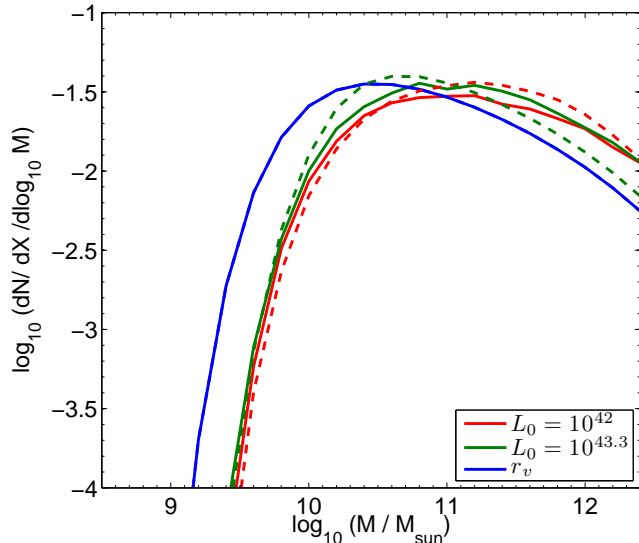


**Figure 11.** The contribution of different mass ranges to the incidence rate of DLAs/emitters ( $d^2N/dX/d\log_{10} M$ ). The same models are shown as in Figure 9. The majority of DLAs/emitters have masses in the range  $10^{10} - 10^{12} M_{\odot}$ . We refer the reader to BH09 for a comparison of our prediction of  $d^2N/dX/d\log_{10} M$  to that of numerical simulations.

Ly $\alpha$  emission was made in BH09. It is thus gratifying that our modeling here with Ly $\alpha$  radiative transfer through inflowing/outflowing distributions of neutral hydrogen in the emitters for which the radial profile is constrained by the observed column density distribution is able to still fit the luminosity function and size distribution of the emitters as well as the velocity width distribution of DLAs for a specific choice of the scaling of the inflow/outflow velocity with radius. This is a non-trivial result and means that the radiative transfer calculations as constrained by the observed properties of the Rauch et al. emitters and DLAs produce a scaling relation of the sizes of emitters with the masses/circular velocities of their DM host haloes very similar to that assumed by BH09.

#### 4.5 Limitations of the current modelling

Our modelling has a number of limitations and (over-) simplifications that we will discuss in this section. Firstly, we have assumed spherical symmetry throughout. Deviations from a uniform spherical configuration will most likely make escape easier for Ly $\alpha$  photons in certain directions. Similarly, our simple velocity field is certainly an oversimplification. More complex velocity fields may bring photons passing through gas in the outer regions of the halo back toward line centre. This may also increase the spatial extent of the emitter.

We have also ignored radiative transfer outside the virial radius of the halo. This effectively assumes not only that scattering in the outer parts of DM halos is negligible but that the same is true for scattering by the neutral hydrogen contained in the IGM. Whether these are reasonable assumptions will depend both on the poorly constrained distribution of neutral hydrogen in the outer parts of low-mass

DM halos and on the bulk motion of the scattering gas relative to the IGM (see e.g. Santos (2004)).

We have furthermore not modelled the effect of ionising radiation, either from external or internal sources of ionising photons, except by reducing the amount of neutral hydrogen within the virial radius of the DM halos below its cosmic value, ostensibly due to the effects of the UV background. More sophisticated modelling should take into account the self-shielding of the gas against the meta-galactic UV background self-consistently. We have checked here that the radius at which the gas is able to maintain neutrality by self-shielding is  $\gtrsim r_{\text{emission}}$ , the size of the emission region at the flux level of the Rauch et al. emitters as defined in Section 4.3. The meta-galactic UV background should thus have little effect on the size of the Ly $\alpha$  emission region predicted by our modelling. Note, however, that this will not be the case anymore at fainter flux levels as the neutral hydrogen density/column density will drop sharply outside the region able to self-shield.

Internal sources of ionising stars such as stars would reduce the neutral fraction of the gas, and in an inhomogeneous manner. Neither stars nor the UV background are expected to significantly ionise the bulk of the neutral gas in the proto-galaxies studied here — these are the sites of DLAs after all. Spatially extended star formation is likely to increase the production of Ly $\alpha$  at large radii, possibly increasing the observed size of the emitters.

Finally, we have also ignored the effects of dust. Our assumption of a negligible effect of dust may not be unreasonable as DLAs are known to have a rather small dust content (Wolfe, Gawiser, & Prochaska 2005) and the escape fraction for Ly $\alpha$  emission appears to increase strongly towards unity with decreasing stellar mass of the emitters (Ono et al. 2009). The recent modelling of Ly $\alpha$  radiative transfer by Laursen, Sommer-Larsen, & Andersen (2009) including dust also suggest that for the majority of DLAs, with their rather low metallicity which are hosted by rather low mass halos, the effect of dust is probably not too important. Note however that there are counter-examples. As shown by Atek, Schaerer, & Kunth (2009), models with almost complete absorption of dust can explain the fact that the expected Ly $\alpha$  emission from the star formation in IZw 18 appears to be entirely absorbed despite a rather modest reddening. As discussed in section 3.1.1, the presence of dust may actually be (partially) responsible for the smaller than unity duty cycle which we require to fit the luminosity function. Note also that the effect of dust should depend sensitively on the clumpiness of the neutral gas (Hansen & Oh 2006).

## 5 CONCLUSIONS

We have used a Monte-Carlo radiative transfer code to model the spatial and frequency distribution of the Ly $\alpha$  emission due to star formation in (proto-)galaxies at the centre of DM halos with masses of  $10^{9.5}$  to  $10^{12} M_{\odot}$  for a range of assumptions for the spatial distribution and the dynamical state of neutral hydrogen. DM halos in this mass range had been previously identified as the likely hosts of DLAs and the recently detected population of faint spatially extended Ly $\alpha$  emitters. Our main results are the following:

- As previously found by other authors, the spectral shape of the Ly $\alpha$  emission from star formation in galaxies for which the dynamics of neutral hydrogen is dominated by infall/outflow is characterized by a strong blue/red peak, occasionally accompanied by a weaker red/blue peak. The spectral shape is very sensitive to the spatial distribution, velocity structure and (to a smaller extent) the temperature structure of the gas. The larger central column densities in the more massive galaxies/halos make escape of the Ly $\alpha$  photons more difficult. The photons must then scatter further in frequency and space and thus emerge with a larger frequency shift and the emission extends to larger radii. Larger bulk motions lead to more energy per scattering being transferred between the photons and the gas. This results in a larger frequency shift of the dominant spectral peak and a larger contrast between the strong and weak spectral peak.

- The surface brightness profiles for photons emitted at the centre of the halos show a central peak with wings extending as far as our assumed neutral hydrogen distribution as long as the column density of neutral hydrogen exceeds about  $\sim 10^{16} \text{ cm}^{-2}$ . The spatial profile of the emission is likewise sensitive to the spatial distribution, velocity and temperature structure of the gas. The spatial distribution is significantly more centrally peaked when the amplitude of the bulk motions increase toward the centre of the halo.

- Expanding shells of neutral hydrogen similar to those invoked to explain the Ly $\alpha$  emission from LBGs produce spectra with one or more prominent red peaks. The surface brightness profiles are very flat, remaining essentially constant for 75% of the radius of the shell. This appears at odds with the observed profiles of the R08 emitters, almost all of which show a central peak.

- Our modelling simultaneously reproduces the column density distribution of the neutral hydrogen and the velocity width of the associated low ionisation metal absorption of DLAs, as well as the size distribution and the luminosity function of the Rauch et al. emitters if we assume i) that absorbers and emitters are hosted by DM halos that retain about 20% of the cosmic baryon fraction in the form of neutral hydrogen, with a spatial distribution which follows a NFW profile with concentration parameter  $\sim 7$  times larger than that of the dark matter, ii) that absorbers and emitters are hosted by DM halos with virial velocities  $\gtrsim 50 \text{ km s}^{-1}$ , and iii) that the central Ly $\alpha$  emission due to star formation has a duty cycle of  $\sim 25\%$  and the luminosity is proportional to the mass of neutral hydrogen in the DM halos.

- The DM halos that contribute most to the incidence rate of DLAs have masses in the range  $M \sim 10^{9.5} - 10^{12} M_{\odot}$  and virial velocities in the range of 35 to 230  $\text{km s}^{-1}$ . The lower cut-off is mainly determined by the rather sharp decrease in the velocity width distribution of the associated low-ionization metal absorption in DLAs at velocity width  $\lesssim 30 \text{ km s}^{-1}$  but may also be reflected in the turn-over of the Ly $\alpha$  luminosity function at the faintest fluxes. The DM host halo masses are significantly smaller than those inferred for  $L_*$  LBGs, consistent with the much higher space density of the faint emitters.

The success of our detailed Ly $\alpha$  radiative transfer modelling in explaining the observed properties of both DLAs and the faint Rauch et al emitters with a consistent set

of assumptions further strengthens the suggestion that the faint emitters are indeed the long-searched for host galaxies of DLA/LLs. Together with our modelling, the observed properties of the faint emitters should thus provide robust estimates not only of the space density, Ly $\alpha$  luminosity and extent of the gas distribution but also of the masses of the DM halos, the duty cycle of star formation and the spatial profile and kinematics of the gas distribution of a statistically representative sample of DLA host galaxies. The current ultra-deep spectroscopic surveys in the HUDF and HDF should soon provide important additional information on the stellar content and possibly also dust content of these objects which will allow to further test the nature of what are almost certainly the building blocks of typical present-day galaxies like our own.

## ACKNOWLEDGMENTS

LAB is supported by an Overseas Research Scholarship and the Cambridge Commonwealth Trust. We thank Richard Bower and Bob Carswell for comments and the referee for a helpful report which has improved the manuscript.

## REFERENCES

- Adams T. F., 1971, *ApJ*, 168, 575
- Adams T. F., 1972, *ApJ*, 174, 439
- Ahn S.-H., Lee H.-W., Lee H. M., 2000, *JKAS*, 33, 29
- Ahn S.-H., Lee H.-W., Lee H. M., 2001, *ApJ*, 554, 604
- Ahn S.-H., Lee H.-W., Lee H. M., 2002, *ApJ*, 567, 922
- Atek H., Schaerer D., Kunth D., 2009, *A&A*, 502, 791
- Auer L. H., 1968, *ApJ*, 153, 783
- Avery L. W., House L. L., 1968, *ApJ*, 152, 493
- Barnes L. A., Haehnelt M. G., 2009, *MNRAS*, 397, 511
- Birnboim Y., Dekel A., 2003, *MNRAS*, 345, 349
- Bonilha J. R. M., Ferch R., Salpeter E. E., Slater G., Noerdlinger P. D., 1979, *ApJ*, 233, 649
- Bullock J. S., Kolatt T. S., Sigad Y., Somerville R. S., Kravtsov A. V., Klypin A. A., Primack J. R., Dekel A., 2001, *MNRAS*, 321, 559
- Cantalupo S., Porciani C., Lilly S. J., Miniati F., 2005, *ApJ*, 628, 61
- Caroff L. J., Noerdlinger P. D., Scargle J. D., 1972, *ApJ*, 176, 439
- Cooke J., Wolfe A. M., Gawiser E., Prochaska J. X., 2006, *ApJ*, 652, 994
- Dijkstra M., Haiman Z., Spaans M., 2006, *ApJ*, 649, 14
- Dijkstra M., Loeb A., 2009, *arXiv*, arXiv:0902.2999
- Gould A., Weinberg D. H., 1996, *ApJ*, 468, 462
- Haehnelt M. G., Steinmetz M., Rauch M., 1998, *ApJ*, 495, 647
- Haehnelt M. G., Steinmetz M., Rauch M., 2000, *ApJ*, 534, 594
- Hansen M., Oh S. P., 2006, *MNRAS*, 367, 979
- Harrington J. P., 1973, *MNRAS*, 162, 43
- Hummer D. G., 1962, *MNRAS*, 125, 21
- Kereš D., Katz N., Weinberg D. H., Davé R., 2005, *MNRAS*, 363, 2
- Kereš D., Katz N., Fardal M., Davé R., Weinberg D. H., 2009, *MNRAS*, 375



- Laursen P., Razoumov A. O., Sommer-Larsen J., 2009, *ApJ*, 696, 853
- Laursen P., Sommer-Larsen J., Andersen A. C., 2009, *arXiv*, arXiv:0907.2698
- Loeb A., Rybicki G. B., 1999, *ApJ*, 524, 527
- Macciò A. V., Dutton A. A., van den Bosch F. C., Moore B., Potter D., Stadel J., 2007, *MNRAS*, 378, 55
- Maller A. H., Bullock J. S., 2004, *MNRAS*, 355, 694
- Nagamine K., Wolfe A. M., Hernquist L., Springel V., 2007, *ApJ*, 660, 945
- Navarro J. F., Frenk C. S., White S. D. M., 1996, *ApJ*, 462, 563
- Natta A., Beckwith S., 1986, *A&A*, 158, 310
- Neufeld D. A., 1990, *ApJ*, 350, 216
- O’Meara J. M., Prochaska J. X., Burles S., Prochter G., Bernstein R. A., Burgess K. M., 2007, *ApJ*, 656, 666
- Ono Y., et al., 2009, *arXiv*, arXiv:0911.2544
- Osterbrock D. E., 1962, *ApJ*, 135, 195
- Panagia N., Ranieri M., 1973, *A&A*, 24, 219
- Pettini M., Steidel C. C., Adelberger K. L., Dickinson M., Gialalisco M., 2000, *ApJ*, 528, 96
- Pettini M., Rix S. A., Steidel C. C., Adelberger K. L., Hunt M. P., Shapley A. E., 2002, *ApJ*, 569, 742
- Pontzen A., et al., 2008, *MNRAS*, 390, 1349
- Prochaska J. X., Wolfe A. M., 1997, *ApJ*, 487, 73
- Prochaska J. X., Wolfe A. M., 2009, *ApJ*, 696, 1543
- Quider A. M., Pettini M., Shapley A. E., Steidel C. C., 2009, *MNRAS*, 398, 1263
- Rauch M., et al., 2008, *ApJ*, 681, 856
- Razoumov A. O., Norman M. L., Prochaska J. X., Sommer-Larsen J., Wolfe A. M., Yang Y.-J., 2008, *ApJ*, 683, 149
- Rybicki G. B., Lightman A. P., 1979, *rpa..book*
- Santos M. R., 2004, *MNRAS*, 349, 1137
- Schaerer D., Verhamme A., 2008, *A&A*, , 480, 369
- Sheth R. K., Tormen G., 2002, *MNRAS*, 329, 61
- Tasitsiomi A., 2006, *ApJ*, 645, 792
- Tescari E., Viel M., Tornatore L., Borgani S., 2009, *MNRAS*, 397, 411
- Unno W., 1952, *PASJ*, 4, 100
- Verhamme A., Schaerer D., Maselli A., 2006, *A&A*, 460, 397
- Verhamme A., Schaerer D., Atek H., Tapken C., 2008, *A&A*, 491, 89
- Veilleux S., Cecil G., Bland-Hawthorn J., 2005, *ARA&A*, 43, 769
- Wechsler R. H., Bullock J. S., Primack J. R., Kravtsov A. V., Dekel A., 2002, *ApJ*, 568, 52
- Wolfe A. M., Gawiser E., Prochaska J. X., 2005, *ARA&A*, 43, 861
- Wolfe A. M., Chen H.-W., 2006, *ApJ*, 652, 981
- Zanstra H., 1949, *BAN*, 11, 1
- Zheng Z., Miralda-Escudé J., 2002, *ApJ*, 568, L71
- Zheng Z., Miralda-Escudé J., 2002, *ApJ*, 578, 33

## APPENDIX A: Ly $\alpha$ RADIATIVE TRANSFER ALGORITHM

### A1 Structure of the Monte-Carlo Code

The details of each step in our Monte Carlo code for Ly $\alpha$  RT are outlined below — throughout,  $R_i$  (for  $i = 1, 2, 3, \dots$ )

denotes a random number generated uniformly between 0 and 1.

- 1.) We begin by specifying, as a function of position,  $\mathbf{r}$ 
  - $n_{\text{HI}}(\mathbf{r})$ , the number density of HI,
  - $\epsilon(\mathbf{r})$ , the Ly $\alpha$  emissivity (in photons/s/cm<sup>3</sup>),
  - $\mathbf{v}_b(\mathbf{r})$ , the bulk velocity field of HI, and
  - $T(\mathbf{r})$ , the temperature of HI.

For the modelling in this paper, these quantities are discussed in Section 3.1.

- 2.) We generate a photon at an initial position  $\mathbf{r}_i$  according to the emissivity. We then choose the photon’s initial direction  $\hat{\mathbf{n}}$  from an isotropic distribution,

$$\hat{\mathbf{n}} = (\sin \theta \cos \phi, \sin \theta \sin \phi, \cos \theta) \quad (\text{A1})$$

where

$$\theta = \cos^{-1}(2R_1 - 1) \quad (\text{the polar angle}), \quad (\text{A2})$$

$$\phi = 2\pi R_2 \quad (\text{the azimuthal angle}). \quad (\text{A3})$$

We generate the photon’s initial frequency as follows. The emission (and absorption) profile in the rest frame of the emitting atom is assumed to be Lorentzian,

$$\phi_L(\nu) = \frac{\Delta\nu_L/2\pi}{(\nu - \nu_0)^2 + (\Delta\nu_L/2)^2}, \quad (\text{A4})$$

where  $\nu_0 = 2.47 \times 10^{15}$  Hz is the central Ly $\alpha$  frequency and  $\Delta\nu_L = 9.936 \times 10^7$  Hz is the natural line width. We take into account the thermal Doppler broadening with an Maxwell-Boltzmann (MB) distribution of the velocity of the scattering atoms. The line profile can then be written as an average of the Lorentz profile over the atoms’ velocities,

$$\phi(\nu) = \int_{-\infty}^{\infty} \phi_L\left(\nu - \frac{\nu_0 v_z}{c}\right) \frac{1}{v_{\text{th}}\sqrt{\pi}} \exp\left(-\frac{v_z^2}{v_{\text{th}}^2}\right) dv_z \quad (\text{A5})$$

$$\Rightarrow \phi(x) = \frac{1}{\Delta\nu_D\sqrt{\pi}} H(a, x), \quad (\text{A6})$$

where the argument of  $\phi_L$  takes into account the Doppler shift in the frequency of the photon as seen by an atom with velocity component  $v_z$  in the direction of the photon’s motion. The other quantities are

$$v_{\text{th}} = \left(\frac{2kT}{m}\right)^{1/2} = 12.85 \text{ km s}^{-1} \left(\frac{T}{10^4 \text{ K}}\right)^{1/2}, \quad (\text{A7})$$

$$a = \frac{\Delta\nu_L}{2\Delta\nu_D} = 4.693 \times 10^{-4} \left(\frac{T}{10^4 \text{ K}}\right)^{-1/2}, \quad (\text{A8})$$

$$\Delta\nu_D = \left(\frac{v_{\text{th}}}{c}\right) \nu_0, \quad (\text{A9})$$

$$x = \frac{\nu - \nu_0}{\Delta\nu_D}, \quad (\text{A10})$$

the thermal velocity dispersion, relative line width, Doppler frequency width and frequency displacement in units of  $\Delta\nu_D$ , respectively. We will use  $x$  as our frequency variable. We have also made use of the *Voigt function*,

$$H(a, x) \equiv \frac{a}{\pi} \int_{-\infty}^{\infty} \frac{e^{-y^2}}{(x - y)^2 + a^2} dy. \quad (\text{A11})$$

The Voigt function can be approximated as a Doppler core and Lorentz wings,

$$H(a, x) \sim \begin{cases} e^{-x^2}, & |x| < x_c \quad (\text{core}), \\ \frac{a}{\sqrt{\pi}x^2}, & |x| > x_c \quad (\text{wing}). \end{cases} \quad (\text{A12})$$

The transition between the two occurs at a ‘critical’ frequency  $x_c$ , defined as the solution to  $e^{-x_c^2} = a/\sqrt{\pi}x_c^2$ . For  $T = 10^4$  K, we have  $x_c \approx 3.255$ . We will use the approximation to the Voigt function given in Tasitsiomi (2006).

Equation (A5) assumes that the “laboratory frame” (in which we are measuring the photon’s frequency) is the same as the fluid rest frame. In order to take account of the bulk fluid velocity, we replace the frequency in the lab frame,  $x$ , with the frequency as seen by the fluid,

$$\bar{x} = x - \frac{\mathbf{v}_b \cdot \hat{\mathbf{n}}}{v_{\text{th}}}. \quad (\text{A13})$$

In practice, the photons are very likely to be emitted close to line centre, and because the photons suffers a large number of resonant scatterings, any “memory” of the initial frequency is quickly erased (DHS06). Thus, we will usually inject all photons at line centre in the fluid frame ( $\bar{x} = 0$ ).

3.) The distance travelled depends on the optical depth. The probability that the photon propagates a physical distance corresponding to an optical depth between  $\tau$  and  $\tau + d\tau$  is  $e^{-\tau} d\tau$ . We choose an optical depth for the photon from this distribution,

$$\tau = -\ln(R_3). \quad (\text{A14})$$

To find the physical distance travelled, we perform the following line integral, solving for  $s_f$ ,

$$\tau_x = \int_0^{s_f} \sigma_x(\mathbf{r}(s)) n_{\text{HI}}(\mathbf{r}(s)) ds, \quad (\text{A15})$$

where  $\mathbf{r}(s) = \mathbf{r}_i + \hat{\mathbf{n}}s$  is the path travelled by the photon, and  $\sigma_x$  is the scattering cross-section of Ly $\alpha$  photons,

$$\sigma_x = f_{12} \pi c r_e \phi(x) \quad (\text{A16})$$

and  $f_{12} = 0.4167$  is the Ly $\alpha$  oscillator line strength while  $r_e = 2.81794 \times 10^{-13}$  cm is the classical electron radius. It is worth noting how the integrand depends on position. The most obvious dependence is that of a spatially varying density  $n_{\text{HI}}(\mathbf{r})$ . The dependence of  $\sigma_\nu$  is two-fold. Firstly, in case of a spatially-varying bulk velocity,  $\sigma_\nu(\phi(\bar{x}(\mathbf{v}_b(\mathbf{r}))))$ . Secondly, if  $T$  depends on position, then so will both  $x$  and  $a$  in  $\phi(x)$  via  $\Delta\nu_D$  and  $v_{\text{th}}$ .

Once  $s_f$  is found, the position of the next scattering is  $\mathbf{r} = \mathbf{r}_i + \hat{\mathbf{n}}s_f$ . If this is outside the HI region, then the algorithm is terminated.

4.) Next we choose the velocity of the scattering atom. Naively, one might think that this step involves generating the three components of the atom’s velocity from the Maxwell-Boltzmann distribution. However, we are choosing the velocity of an atom *given* that it scatters a photon with frequency  $x$ . We can therefore divide the velocity of the atom into one component parallel ( $v_{\parallel}$ ) and two components perpendicular to the direction of motion of the photon ( $v_{\perp 1}$ ,  $v_{\perp 2}$ ). The two perpendicular components do not alter the frequency of the photon as seen by the atom, and are thus chosen from a Maxwell-Boltzmann distribution. From Equations (A5)-(A11) it can be seen that the probability that a photon with frequency  $x$  scatters off an atom with velocity

(along the direction of propagation of the photon) between  $v_{\parallel}$  and  $v_{\parallel} + dv_{\parallel}$  is,

$$f(u_{\parallel}) du_{\parallel} = \frac{a}{\pi} \frac{e^{-u_{\parallel}^2}}{(x - u_{\parallel})^2 + a^2} \frac{1}{H(a, x)} du_{\parallel}, \quad (\text{A17})$$

where  $u_{\parallel} = v_{\parallel}/v_{\text{th}}$ . A scheme for generating random numbers from this distribution is given in Zheng & Miralda-Escudé (2002).

5.) Now that we have calculated  $\mathbf{v}_a$ , the velocity of the atom that scatters the photon, we perform a Lorentz transform into the rest frame of the atom. In this frame, we assume that the frequency of the scattered photon differs from the frequency of the incident photon only by the recoil effect (Rybicki & Lightman 1979, pg. 196). We choose a new direction for the photon. Our code can incorporate either an isotropic or a dipole distribution for the direction of the re-emitted photon. The results are insensitive to the choice. We then transform back into the laboratory frame. At speeds much less than  $c$  we have, for an initial photon direction  $\hat{\mathbf{n}}$ , and having chosen a final photon direction  $\hat{\mathbf{n}}_f$ , that the final frequency of the photon is,

$$x_f = x - \frac{\hat{\mathbf{n}} \cdot \mathbf{v}_a}{v_{\text{th}}} + \frac{\hat{\mathbf{n}}_f \cdot \mathbf{v}_a}{v_{\text{th}}} + \frac{h\Delta\nu_D}{2kT}(\hat{\mathbf{n}} \cdot \hat{\mathbf{n}}_f - 1). \quad (\text{A18})$$

In general, the final term, known as the recoil term (Adams 1971), is negligible for the modelling in this paper.

We now return to step (iii) and repeat it until the photon escapes the HI region.

Once the photon escapes the region, its properties (frequency, angle of escape etc.) are recorded. We then return to step (ii) and generate another photon.

Our code incorporates the presence of a cosmic abundance of deuterium, following the method presented in DHS06. Adding deuterium has only a minimal effect.

## A2 Accelerating The Code

Monte Carlo Ly $\alpha$  RT codes like the one used here can be significantly accelerated by skipping scatterings in the core of the line profile. We define the core-to-wing transition to occur at a critical frequency  $x_{\text{crit}}$ , which is not the same as  $x_c$ . Whenever a photon is in the core  $|x| < x_{\text{crit}}$ , we force it into the wing by choosing the scattering atom’s velocity to be large. We follow the method presented in Ahn, Lee, & Lee (2002), DHS06, choosing the perpendicular components of the atom’s velocity such that  $u_{\perp 1}^2 + u_{\perp 2}^2 \geq x_{\text{crit}}^2$ .

We choose the value of  $x_{\text{crit}}$  by requiring that, for a uniform sphere, less than a fraction  $f$  of the photons that emerge have  $|x| < x_{\text{crit}}$ . Using the analytic solution for the emergent spectrum of a sphere (DHS06, Equation (9)), this gives,

$$x_{\text{crit}} = \left( \sqrt{\frac{54}{\pi^3}} a \tau_0 \tanh^{-1} f \right)^{\frac{1}{3}}, \quad (\text{A19})$$

where  $\tau_0$  is the line-centre optical depth from the centre to the edge. We find that setting  $f = 0.01$  up to  $\max(x_{\text{crit}}) = 3$  ( $\approx x_c$ ) gives an acceptable compromise between speed and accuracy. This procedure can accelerate the code by several orders of magnitude, e.g. for a static sphere with  $\tau_0 = 10^7$ , the code is accelerated by a factor of more than a thousand.



### A3 Spherically Symmetric Shells

In cases where  $n_{\text{HI}}$ ,  $T$  and/or  $v_b$  have a complicated dependence on  $r$ , solving for  $s_f$  in Equation (A15) can be computationally expensive. In spherical symmetry, we use a similar approach to DHS06, dividing the sphere into shells of uniform density. Within each shell, the integral (A15) becomes trivial,  $\tau = s_f \sigma_x n_{\text{HI}}(r_{\text{shell}})$ . If the edge of a shell is reached, the optical depth to the edge of the shell is subtracted from  $\tau$  and a new  $s_f$  is calculated using the new value of  $r_{\text{shell}}$ . We space the shells so that each shell has equal column density. We choose the number of shells to keep the frequency dispersion within each shell small compared to the change in frequency as the photon crosses a shell; 1000 shells are usually sufficient.

## APPENDIX B: THE EFFECT OF TEMPERATURE AND VELOCITY AMPLITUDE

In this section, we will consider the effect of altering the gas temperature and amplitude of the bulk velocity. For this section, the fiducial model is different to that in Section 3.1.4:  $(z, M_v, c_0, f_e, v_{\text{amp}}, T) = (3, 10^{11} M_{\odot}, 3.5, 1, v_c, 10^4 \text{ K})$ .

### B1 The effect of the velocity profile

In this section, we consider the effect of decreasing  $v_{\text{amp}}$ . The results are shown in Figure B1. Setting  $v_{\text{amp}} = 0$  would result in  $J(x)$  being symmetric about  $x = 0$  (ignoring the small effects of deuterium and recoil). This tendency is seen clearly in both of the left plots. These plots also show that photons emerge bluer as the velocity of infall increases. Photons gain energy from head-on collisions with atoms, and the more energetic the atoms, the more energy is transferred between photons and gas.

The surface brightness plots show that the emission becomes more extended as the velocity is reduced. A rather flat surface brightness profile is characteristic of a uniform, static HI sphere. This is because the bulk velocity can give photons a “free ride” through the halo, Doppler shifting their frequency away from line centre in the fluid frame without changing  $x$  in the laboratory frame. In the  $\alpha = -0.5$  case, the peak surface brightness is reduced by almost 2 orders of magnitude by this effect. It is also worth noting that the smaller  $v_{\text{amp}}$  is, the less the dependence of the profile on  $\alpha$ .

### B2 Temperature

The effect of altering the temperature is shown in Figure B2. Note that the spectrum is given as a function of velocity ( $v \equiv -x v_{\text{th}}$ ), as  $x$  itself is temperature dependent ( $\propto 1/\sqrt{T}$ ). For the  $\alpha = -0.5$  case, there is no dependence on the temperature because the photon begins its flight with a frequency (in the fluid frame) in the scattering wings, and is unlikely to return to the Doppler core. Remember that the scattering cross-section does not depend on  $T$  in the Lorentz wing of the profile. In the  $\alpha = 1$  case, the effect of temperature is minimal. The red peak disappears at lower temperatures due to the corresponding increase in the scattering cross-section,  $\sigma_x \propto 1/\Delta\nu_D \propto 1/\sqrt{T}$ , when  $x$  is small.

This paper has been typeset from a T<sub>E</sub>X/L<sup>A</sup>T<sub>E</sub>X file prepared by the author.

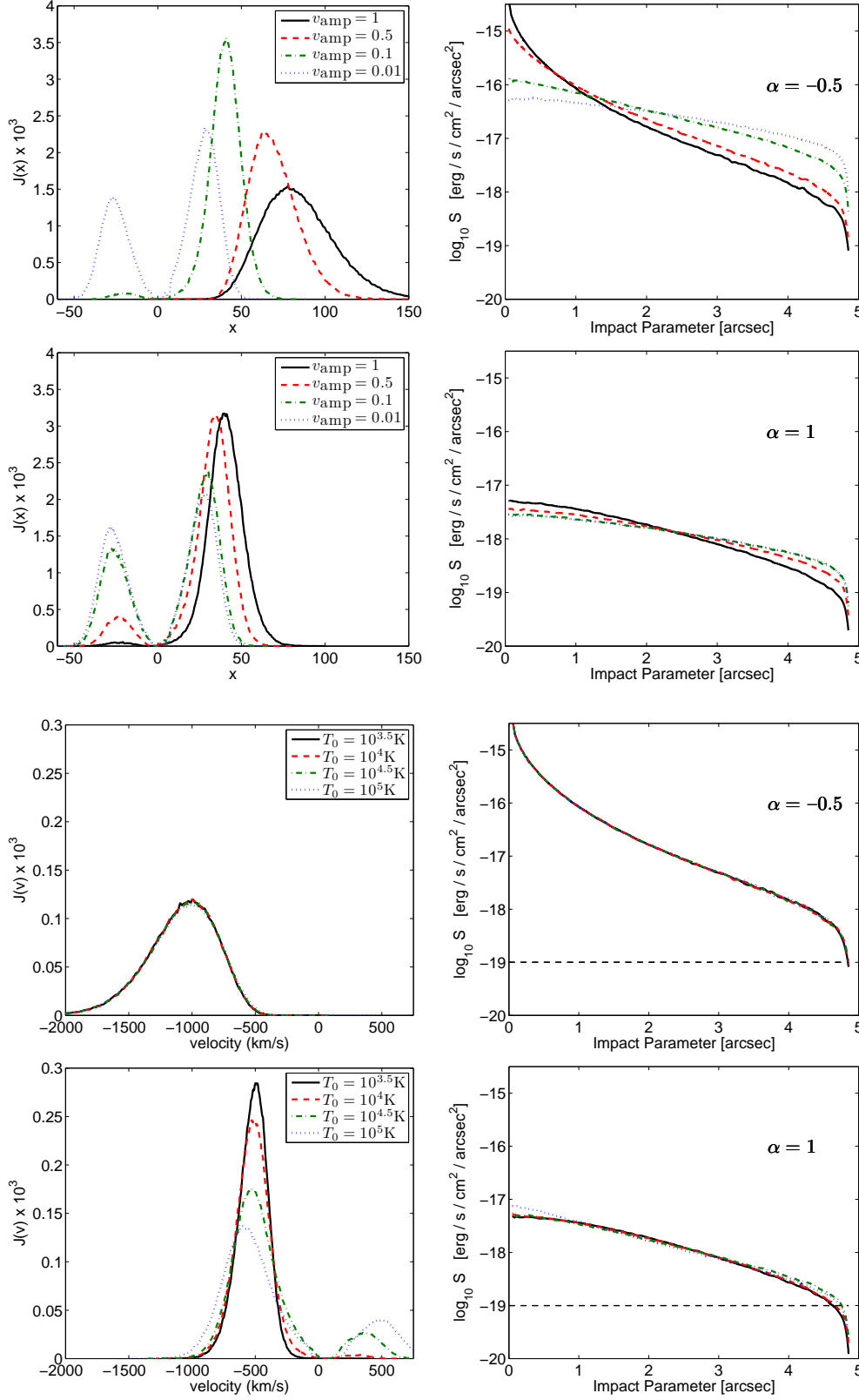


**Figure B1.** Spectra (left panels) and surface brightness profiles (right panels) for DLAs in halos with  $v_{\text{amp}}$  as given in the legend in units of the virial velocity. The top panels are for  $\alpha = -0.5$ , for which  $L_{\text{Ly}\alpha} = 1.1 \times 10^{44} \text{ erg s}^{-1}$ . The bottom panels are for  $\alpha = 1$ , for which  $L_{\text{Ly}\alpha} = 5.5 \times 10^{42} \text{ erg s}^{-1}$ . As the velocity decreases, the spectrum begins to resemble the double-peaked static sphere profile. The surface brightness profile flattens as the velocity decreases — where the bulk velocity is low, the photons must random walk out of the Doppler core by scattering; they will not be given a “free ride” by the fluid flow.

**Figure B2.** Spectra and surface brightness profiles as a function of *velocity* for DLAs in haloes with temperature  $T_0$  as given in the legend. The top panels are for  $\alpha = -0.5$ , for which  $L_{\text{Ly}\alpha} = 1.1 \times 10^{44} \text{ erg s}^{-1}$ . The bottom panels are for  $\alpha = 1$ , for which  $L_{\text{Ly}\alpha} = 5.5 \times 10^{42} \text{ erg s}^{-1}$ . For the  $\alpha = -0.5$  case, there is no dependence on the temperature because the photon begins its flight with frequency (in the fluid frame) in the scattering wings, and is unlikely to return to the Doppler core. In the  $\alpha = 1$  case, the effect of temperature is minimal. The red peak disappears at lower temperatures due to the corresponding increase in the scattering cross-section,  $\sigma_x \propto 1/\Delta\nu_D \propto 1/\sqrt{T}$ , when  $x$  is small.